

Enhanced stability of lead-free double perovskite $\text{Cs}_2\text{Na}_{1-x}\text{Bi}_{1-x}\text{Mn}_{2x}\text{Cl}_6$ microcrystals and their optoelectronic devices under high humidity environment by SiO_2 encapsulation

Jindou Shi ^a, Minqiang Wang ^{a,*}, Chen Zhang ^a, Junnan Wang ^a, Yun Zhou ^a, Youlong Xu ^a, N.V. Gaponenko ^b

^a Electronic Materials Research Laboratory, Key Laboratory of the Ministry of Education International Center for Dielectric Research & Shannxi Engineering Research Center of Advanced Energy Materials and Devices, Xi'an Jiaotong University, Xi'an 710049, PR China

^b Belarusian State University of Informatics and Radioelectronics, P. Browki 6, Minsk 220013, Belarus



ARTICLE INFO

Article history:

Received 29 December 2022
Received in revised form
20 February 2023
Accepted 25 February 2023
Available online 23 March 2023

KEYWORDS:

Lead-free double perovskite
Stability
High humidity environment
 SiO_2 encapsulation
 $\text{Cs}_2\text{Na}_{0.8}\text{Bi}_{0.8}\text{Mn}_{0.4}\text{Cl}_6/\text{SiO}_2$ MCs

ABSTRACT

The current studies on lead-free double perovskites (DPs) have mainly focused on the optimization of their optical properties, while less attention has been paid to their optical stability under high humidity environment. However, optoelectronic devices will inevitably be exposed to high humidity environment in practical applications so that investigating the optical stability of lead-free DPs under high humidity environment will be especially important for its subsequent development. We prepared lead-free DP $\text{Cs}_2\text{Na}_{1-x}\text{Bi}_{1-x}\text{Mn}_{2x}\text{Cl}_6$ microcrystals (MCs) with different Mn^{2+} content by the solution method at room temperature, where the photoluminescence quantum yield (PLQY) of $\text{Cs}_2\text{Na}_{0.8}\text{Bi}_{0.8}\text{Mn}_{0.4}\text{Cl}_6$ MCs achieved a maximum of 22.3% with 20% doping of Mn^{2+} , subsequently tested for stability under high humidity environment. The results indicated that the structure and fluorescence properties of $\text{Cs}_2\text{Na}_{0.8}\text{Bi}_{0.8}\text{Mn}_{0.4}\text{Cl}_6$ MCs were destroyed after being contacted with water molecules and that $\text{Cs}_2\text{Na}_{0.8}\text{Bi}_{0.8}\text{Mn}_{0.4}\text{Cl}_6$ MCs was subsequently restored again by using hydrochloric acid solution, but its fluorescence was not able to reach initial intensity, which severely affected its application under high humidity environment. Therefore, the encapsulation of $\text{Cs}_2\text{Na}_{0.8}\text{Bi}_{0.8}\text{Mn}_{0.4}\text{Cl}_6$ MCs using water stable and highly transparent SiO_2 was proposed to obtain $\text{Cs}_2\text{Na}_{0.8}\text{Bi}_{0.8}\text{Mn}_{0.4}\text{Cl}_6/\text{SiO}_2$ core-shell MCs, its optical properties were unaffected after stored in aqueous solution for 10 days. The assembled light emitting diode devices kept constant illumination output in harsh environment of 85% relative humidity, which laid a solid foundation for the subsequent development of lead-free DP optoelectronic devices.

© 2023 Elsevier Ltd. All rights reserved.

1. Introduction

In recent years, lead halide perovskites materials were considered as candidates for optoelectronic devices in the future owing to their excellent optical and electronic properties, and they have been extensively investigated in the fields of solar cells, light emitting diodes (LEDs), photodetectors, and so on [1–8]. Unfortunately, the inherent toxicity and instability under environmental conditions of lead halide perovskites cannot be thoroughly eliminated, severely hindering its further development in commercial devices [9–12]. To overcome the toxicity of Pb^{2+} , researchers have

proposed to replace partial or complete Pb^{2+} by using divalent metal cations Sn^{2+} and Ge^{2+} , but they are highly susceptible of being oxidized to Sn^{4+} and Ge^{4+} in the ambient atmosphere, so the strategy of isovalent substitution was risky [13–15]. Subsequently, the synthesis of stable lead-free double perovskites (DPs) by combining monovalent (B^+) and trivalent (B^{3+}) metal cations to heterovalently replace Pb^{2+} attracted much attention, with the general formula $\text{A}_2\text{B}^+\text{B}^{3+}\text{X}_6$ ($\text{A} = \text{Cs}^+, \text{Rb}^+$; $\text{B}^+ = \text{Ag}^+, \text{K}^+, \text{Na}^+, \text{Li}^+$; $\text{B}^{3+} = \text{Bi}^{3+}, \text{Sb}^{3+}, \text{In}^{3+}$; $\text{X} = \text{Cl}^-, \text{Br}^-, \text{I}^-$), which maintained the 3D perovskite structure and charge neutrality, bringing great potential for the subsequent development of their optoelectronic properties [16–18]. However, the current studies have more attention on optimizing the optical behaviors of lead-free DPs and less on their optical stability under high humidity environments, which will be detrimental to its further development in practical applications.

* Corresponding author.

E-mail address: mqwang@xjtu.edu.cn (M. Wang).

Nowadays, multiple preparation routes were reported to acquire different lead-free DP materials [19–21]. Of these, the indirect bandgap $\text{Cs}_2\text{NaBiCl}_6$, as an emerging lead-free DP, has a band edge transition that was parity allowed, but was characterized with weak oscillator strength, which resulted in lower photoluminescence quantum yield (PLQY) that severely limited its application in optoelectronics [22]. It has been claimed that the introduction of long lifetime Mn^{2+} into the lattice of $\text{Cs}_2\text{NaBiCl}_6$ by different synthetic methods can be optimized for its optical properties, enabling it to exhibit orange red photoluminescence (PL) under ultraviolet (UV) excitation [23]. For example, $\text{Cs}_2\text{NaBiCl}_6:\text{Mn}^{2+}$ nanocrystals (NCs) were achieved by doping Mn^{2+} into $\text{Cs}_2\text{NaBiCl}_6$ with high temperature thermal injection, and $\text{Cs}_2\text{NaBiCl}_6:\text{Mn}^{2+}$ microcrystals (MCs) were produced by high temperature chemical reflow, and both exhibited bright orange–red fluorescence emission, suggesting that Mn^{2+} doping was a simple and effective method for enhancing the optical properties of $\text{Cs}_2\text{NaBiCl}_6$ [24,25]. However, optoelectronic materials will inevitably be exposed to some high humidity environments during practical applications [26,27]. The pure phase $\text{Cs}_2\text{AgBiBr}_6$ NCs were found to be self-passivated in aqueous solution forming BiOBr , its crystal structure was severely damaged [28]. Therefore, the investigation into the optical stability of Mn^{2+} -doped $\text{Cs}_2\text{AgBiCl}_6$ under high humidity environment will be an indispensable step in its commercial development process.

In this work, octahedral $\text{Cs}_2\text{Na}_{1-x}\text{Bi}_{1-x}\text{Mn}_{2x}\text{Cl}_6$ MCs doped with different Mn^{2+} content was prepared at room temperature by applying a simple solution method, and they emitted a bright orange–red fluorescence at 585 nm, where the PLQY of $\text{Cs}_2\text{Na}_{0.8}\text{Bi}_{0.8}\text{Mn}_{0.4}\text{Cl}_6$ MCs can be up to 22.3%. Especially, the stability of $\text{Cs}_2\text{Na}_{0.8}\text{Bi}_{0.8}\text{Mn}_{0.4}\text{Cl}_6$ MCs with the best optical properties was tested under high humidity environment, and the results showed that fluorescent emission of $\text{Cs}_2\text{Na}_{0.8}\text{Bi}_{0.8}\text{Mn}_{0.4}\text{Cl}_6$ MCs was rapidly quenched after being contacted with water molecules. Although the PL properties of $\text{Cs}_2\text{Na}_{0.8}\text{Bi}_{0.8}\text{Mn}_{0.4}\text{Cl}_6$ MCs were subsequently recovered by adding the hydrochloric acid (HCl) solution again, the fluorescence was unable to reach its initial intensity, which greatly limited the application of $\text{Cs}_2\text{Na}_{0.8}\text{Bi}_{0.8}\text{Mn}_{0.4}\text{Cl}_6$ MCs under high humidity environment. Therefore, $\text{Cs}_2\text{Na}_{0.8}\text{Bi}_{0.8}\text{Mn}_{0.4}\text{Cl}_6@/\text{SiO}_2$ core-shell MCs were fabricated by encapsulating $\text{Cs}_2\text{Na}_{0.8}\text{Bi}_{0.8}\text{Mn}_{0.4}\text{Cl}_6$ MCs with water-stable and highly transparent SiO_2 , and their structural and optical properties were stabilized after being stored in pure aqueous solution for 10 days. Moreover, the LED devices assembled with $\text{Cs}_2\text{Na}_{0.8}\text{Bi}_{0.8}\text{Mn}_{0.4}\text{Cl}_6@/\text{SiO}_2$ MCs exhibited minimal changes in the corresponding optoelectronic parameters after being stored at 85% relative humidity (RH) for 150 h, which dramatically enhanced the competitiveness of lead-free DP materials for commercial optoelectronic device applications in the future.

2. Results and discussion

Herein, $\text{Cs}_2\text{NaBiCl}_6$ MCs doped with different Mn^{2+} contents were prepared by a simple solution method, and their structures and microscopic morphologies were investigated. The X-ray diffraction (XRD) patterns revealed that all samples were highly crystallized in the DP crystal structure, and their diffraction peaks completely followed the bulk $\text{Cs}_2\text{NaBiCl}_6$ (ICSD: 2738), with no significant secondary phase was observed (Fig. 1a), indicating that the Mn^{2+} had been doped into the $\text{Cs}_2\text{NaBiCl}_6$ MCs. It is known from previous related studies that the electronegativity difference between Mn (1.55) and Cs (0.79) was larger so that the possibility of Mn^{2+} replacing the Cs^+ site during the doping process was lower. Conversely, the ionic radius of Mn^{2+} ($R = 83$ p.m., coordination number, CN = 6) was smaller than that of Na^+ ($R = 102$ p.m.,

CN = 6) and Bi^{3+} ($R = 103$ p.m., CN = 6), it could potentially substitute for both Na^+ and Bi^{3+} . Subsequently, the possibility of ionic substitution was closely evaluated according to defect chemistry, and the acceptable percentage difference between the two ionic radii should be lower than 25% [29]. The substitution relationship can be derived from the following equation:

$$D_r = 100\% \times \frac{[R_m(\text{CN}) - R_d(\text{CN})]}{R_m(\text{CN})} \quad (1)$$

where D_r is the percentage difference in radius, CN is the coordination number. R_m and R_d are the radii of the main cation and the doped cation, respectively. The calculations show that the D_r values between Mn^{2+} with Na^+ (18.63%)/ Bi^{3+} (19.42%) were all lower than the limit value (25%), and the similar D_r values indicated that the exchange potential of Mn^{2+} and Na^+ / Bi^{3+} should be equal. Moreover, first-principle calculations of formation energy suggested that Mn^{2+} could simultaneously replace part of Na^+ and Bi^{3+} to form $\text{Cs}_2\text{Na}_{1-x}\text{Bi}_{1-x}\text{Mn}_{2x}\text{Cl}_6$ (Fig. 1b) [30]. Meanwhile, the magnification of XRD in the 22.5° – 24.0° range indicated that the diffraction peaks of $\text{Cs}_2\text{Na}_{1-x}\text{Bi}_{1-x}\text{Mn}_{2x}\text{Cl}_6$ MCs were shifted toward a higher 2θ angle as the Mn^{2+} content increased (Fig. S1), which just confirmed that Na^+ and Bi^{3+} were replaced by the smaller Mn^{2+} caused to lattice contraction. Subsequently, Raman spectroscopy was applied to probe further the microstructural changes of $\text{Cs}_2\text{Na}_{1-x}\text{Bi}_{1-x}\text{Mn}_{2x}\text{Cl}_6$ MCs as the doping concentration of Mn^{2+} increased (Fig. S2a). Two different vibrational modes can be seen in the Raman spectrum of the pure phase $\text{Cs}_2\text{NaBiCl}_6$ MCs, belonging to the T_{2g} (at 113 cm) mode of $[\text{BiCl}_6]^{3-}$ octahedral bending vibrations and the A_{1g} (at 280 cm) mode of $[\text{BiCl}_6]^{3-}$ octahedral stretching vibrations, respectively [31]. Notably, both the T_{2g} and A_{1g} modes of $\text{Cs}_2\text{Na}_{1-x}\text{Bi}_{1-x}\text{Mn}_{2x}\text{Cl}_6$ MCs gradually shifted toward higher wave numbers when Mn^{2+} was doped (Fig. S2b), which was attributed to the replacement of Bi^{3+} site by smaller Mn^{2+} , resulting in a reduction of the average Mn/Bi–Cl bond length [32]. These results reconfirmed that Mn^{2+} had been doped into $\text{Cs}_2\text{NaBiCl}_6$ MCs, and $\text{Cs}_2\text{Na}_{1-x}\text{Bi}_{1-x}\text{Mn}_{2x}\text{Cl}_6$ MCs preserved the cubic symmetry of $\text{Cs}_2\text{NaBiCl}_6$.

The scanning electron microscope (SEM) images of $\text{Cs}_2\text{Na}_{1-x}\text{Bi}_{1-x}\text{Mn}_{2x}\text{Cl}_6$ MCs with different Mn^{2+} contents ($x = 0.00$ and 0.01) showed that the morphology of the samples before and after doping was uniform (Fig. 1c, e), displaying octahedral MC particles and the surface of each MC particle was very smooth (inset of Fig. 1c, e). Moreover, $\text{Cs}_2\text{Na}_{1-x}\text{Bi}_{1-x}\text{Mn}_{2x}\text{Cl}_6$ MCs under the other doping components ($x = 0.05, 0.10, 0.15, 0.20, 0.25$) also exhibited octahedral MC particles with an average size of approximately $10 \mu\text{m}$ (Fig. S3), indicating that the doping of Mn^{2+} does not trigger a change in crystal morphology. Correspondingly, the transmission electron microscope (TEM) images of $\text{Cs}_2\text{NaBiCl}_6$ MCs and $\text{Cs}_2\text{Na}_{0.99}\text{Bi}_{0.99}\text{Mn}_{0.02}\text{Cl}_6$ MCs indicated that the samples achieved by the solution method were high crystallinity (inset of Fig. 1d, f), with distinct lattices being observable in the high-resolution TEM images (Fig. 1d, f). Where the lattice spacing of the pure phase $\text{Cs}_2\text{NaBiCl}_6$ MCs was 0.38 nm, corresponding to its (220) crystal plane (Fig. 1d). Compared to the pure phase $\text{Cs}_2\text{NaBiCl}_6$ MCs (Fig. S4), the trace amount of Mn elements was detected in the energy-dispersive spectroscopy spectrum analysis result of $\text{Cs}_2\text{Na}_{0.99}\text{Bi}_{0.99}\text{Mn}_{0.02}\text{Cl}_6$ MCs (Fig. 1g), which reflected the high doping efficiency of Mn^{2+} . Finally, the corresponding element mapping images showed a homogeneous distribution of all elements in $\text{Cs}_2\text{Na}_{0.99}\text{Bi}_{0.99}\text{Mn}_{0.02}\text{Cl}_6$ MCs (Fig. 1h), which again supported the formation of alloy MCs. Combined with the above characterization results, it can be concluded that the doping of Mn^{2+} in $\text{Cs}_2\text{NaBiCl}_6$ MCs can be successfully achieved by the simple solution method.

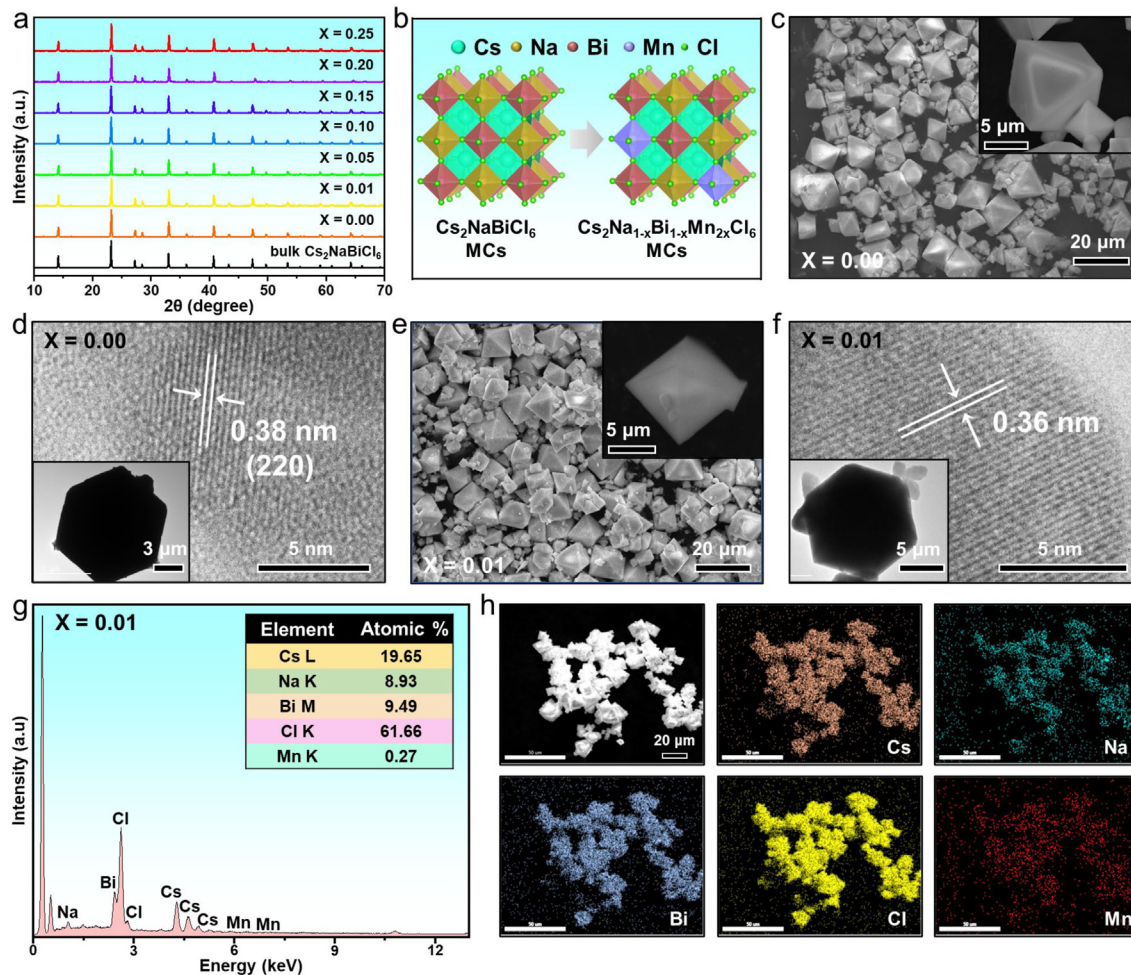


Fig. 1. (a) XRD patterns of $\text{Cs}_2\text{Na}_{1-x}\text{Bi}_{1-x}\text{Mn}_{2x}\text{Cl}_6$ MCs with different Mn^{2+} content, the bottom corresponds to a pure bulk $\text{Cs}_2\text{NaBiCl}_6$ (ICSD: 2738). (b) Schematic diagram of the structure of Mn doped in $\text{Cs}_2\text{NaBiCl}_6$ MCs. SEM (c) and HRTEM (d) images of $\text{Cs}_2\text{NaBiCl}_6$ MCs. SEM (e) and HRTEM (f) images of $\text{Cs}_2\text{Na}_{0.99}\text{Bi}_{0.99}\text{Mn}_{0.02}\text{Cl}_6$ MCs. (g) EDS spectrum and (h) elemental mapping of $\text{Cs}_2\text{Na}_{0.99}\text{Bi}_{0.99}\text{Mn}_{0.02}\text{Cl}_6$ MCs. The inset in (c), (e) show the corresponding single MC images. The inset in (d), (f) show the corresponding TEM images. EDS, energy-dispersive spectroscopy; HRTEM, high-resolution transmission electron microscope; MC, microcrystal; SEM, scanning electron microscope; XRD, X-ray diffraction.

Subsequently, the optical properties of $\text{Cs}_2\text{Na}_{1-x}\text{Bi}_{1-x}\text{Mn}_{2x}\text{Cl}_6$ MCs with different Mn^{2+} content were analyzed closely, enabling their better suitability for optoelectronic devices in the future. The UV visible absorbance spectra of $\text{Cs}_2\text{Na}_{1-x}\text{Bi}_{1-x}\text{Mn}_{2x}\text{Cl}_6$ MCs remained almost unchanged as the doping concentration increased (Fig. 2a), indicating that the doped Mn^{2+} was insensitive to the electronic structure of the host [33]. There are three distinct absorption bands observed in the absorbance spectra of $\text{Cs}_2\text{Na}_{1-x}\text{Bi}_{1-x}\text{Mn}_{2x}\text{Cl}_6$ MCs, which are all related to the $6s^2 \rightarrow 6s1p^1$ transition of the $[\text{BiCl}_6]^{3-}$ octahedra [23,25]. Typically, the antibonding interaction between the Bi 6p and Cl 3p orbitals forms the conduction band minimum, the antibonding interaction between Bi 6s and Cl 3p orbitals forms the valence band maximum [34]. Of these, the double peaks at 318 and 340 nm were assigned to spin forbidden $^1S_0 \rightarrow ^3P_1$ transition, the splitting of this transition being attributed to the dynamic Jahn-Teller effect caused by the coupling of lattice vibrations with empty T_{1u} orbitals with antibonding Bi 6p-Cl 3p character [23]. The absorption peak at 378 nm was assigned to the spin forbidden $^1S_0 \rightarrow ^3P_0$ transition, and the weaker intensity of this peak originated from the spin and parity forbidden nature of the transition [23]. The PL spectra revealed that all $\text{Cs}_2\text{Na}_{1-x}\text{Bi}_{1-x}\text{Mn}_{2x}\text{Cl}_6$ MCs doped with Mn ions displayed a broad PL emission peak at 585 nm (Fig. 2b), which was attributed to the

transfer of excitonic energy from the conduction band to the neighboring Mn^{2+} ionic state. Of these, the Mn^{2+} ionic state acted as an additional channel to receive and accumulate photogenerated excitons, yielding the $^4T_1 \rightarrow ^6A_1$ PL emission (≈ 585 nm) (Fig. 2c) [24,35]. However, the indirect bandgap structure and parity allowed transitions with weak oscillator strength in pure $\text{Cs}_2\text{NaBiCl}_6$ MCs so that no significant PL property was displayed [22]. On the other hand, all the $\text{Cs}_2\text{Na}_{1-x}\text{Bi}_{1-x}\text{Mn}_{2x}\text{Cl}_6$ MCs exhibited bright orange-red emission under UV irradiation as the doping concentration of Mn^{2+} was increased (inset of Fig. 2c), and the corresponding PL intensity and PLQYs values were progressively improved (Fig. 2b and c). Especially, the $\text{Cs}_2\text{Na}_{0.8}\text{Bi}_{0.8}\text{Mn}_{0.4}\text{Cl}_6$ MCs displayed excellent optical emission when the doping ratio of Mn^{2+} reached $x = 0.20$, corresponding the PLQY high up to 22.3%. Unfortunately, the Mn^{2+} content was further lifted ($x = 0.25$), and the corresponding PL intensity and PLQY value were decayed. This phenomenon can be explained by the previously reported PL quenching effect caused with inter-dopant coupling under excessive doping [33], and a similar phenomenon has been observed in Mn^{2+} -doped $\text{Cs}_2\text{NaInCl}_6$ crystals [36]. Finally, in order to probe more deeply into the charge carrier recombination kinetics in Mn^{2+} -doped $\text{Cs}_2\text{NaBiCl}_6$ MCs, their time-resolved PL decay behavior was recorded (Fig. 2d). The results showed that the PL

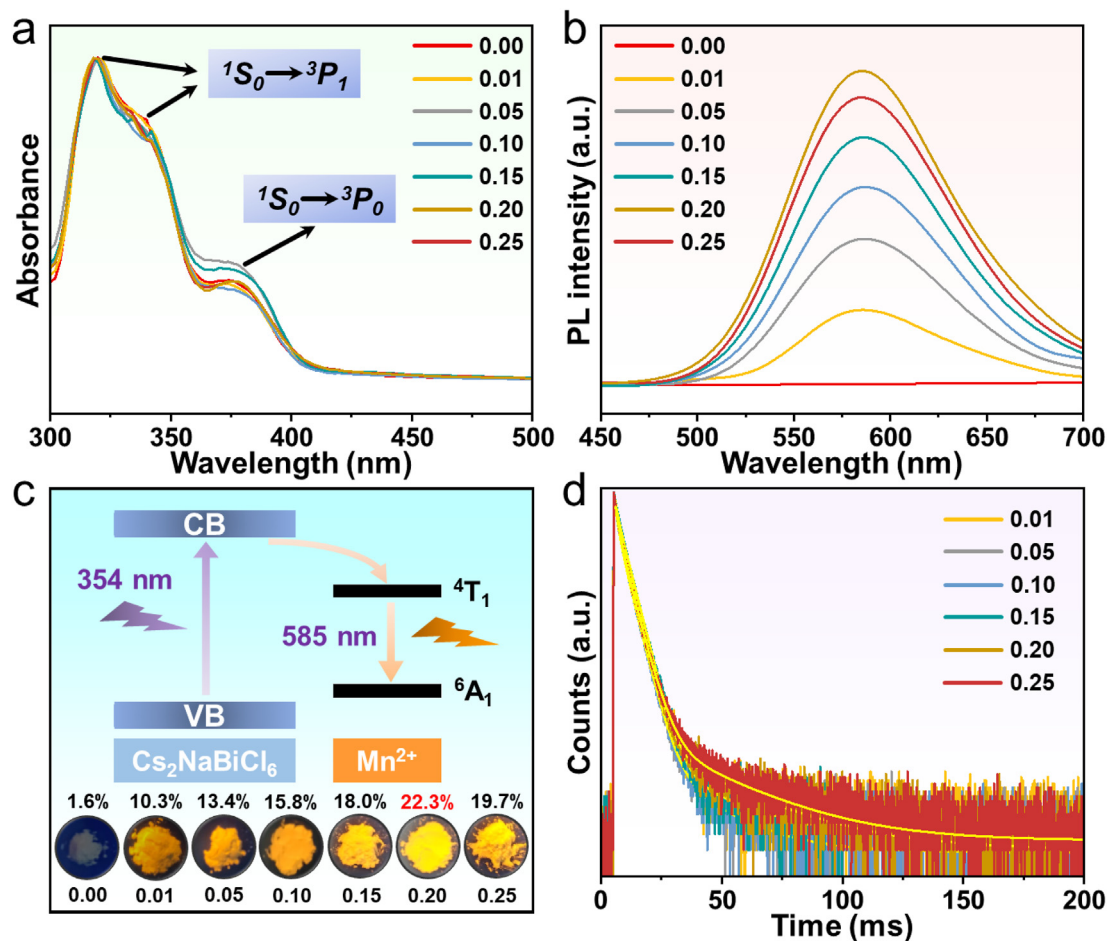
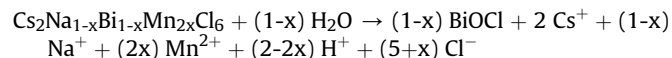


Fig. 2. (a) Absorbance and (b) PL spectra of $\text{Cs}_2\text{Na}_{1-x}\text{Bi}_{1-x}\text{Mn}_{2x}\text{Cl}_6$ MCs with different Mn^{2+} content. (c) Schematic diagram of the luminescence mechanism of $\text{Cs}_2\text{Na}_{1-x}\text{Bi}_{1-x}\text{Mn}_{2x}\text{Cl}_6$ MCs (CB, conduction band; VB, valence band). (d) Time-resolved PL spectra of $\text{Cs}_2\text{Na}_{1-x}\text{Bi}_{1-x}\text{Mn}_{2x}\text{Cl}_6$ MCs doped with Mn^{2+} . The inset in (c) exhibit photographs and PLQYs of $\text{Cs}_2\text{Na}_{1-x}\text{Bi}_{1-x}\text{Mn}_{2x}\text{Cl}_6$ MCs with different Mn^{2+} content under UV light. MC, microcrystal; PL, photoluminescence; PLQY, photoluminescence quantum yield; UV, ultraviolet.

decay curves of $\text{Cs}_2\text{Na}_{1-x}\text{Bi}_{1-x}\text{Mn}_{2x}\text{Cl}_6$ MCs can be well fitted by the bi-exponential decay function, where the shortest average decay lifetime was up to 3.43 ms (Table S1). According to former reported, the decay lifetime of self-trapped exciton state PL emission was approximately within 10^{-6} s [37], so the longer decay lifetime of the $\text{Cs}_2\text{Na}_{1-x}\text{Bi}_{1-x}\text{Mn}_{2x}\text{Cl}_6$ MCs indicated their charge carrier recombination had undergone a more complex process, which exactly matched the luminescence mechanism proposed above (Fig. 2c). Afterward, in order to further expand the application of $\text{Cs}_2\text{Na}_{1-x}\text{Bi}_{1-x}\text{Mn}_{2x}\text{Cl}_6$ MCs in the field of lead-free DP optoelectronics, the $\text{Cs}_2\text{Na}_{0.8}\text{Bi}_{0.8}\text{Mn}_{0.4}\text{Cl}_6$ MCs with the most outstanding optical properties was selected for subsequent studies by the above comparison.

In practical applications, optoelectronic devices will inevitably be exposed to some high humidity environments, which will bring new challenges to the water resistance of their core fluorescent materials. Therefore, further exploring the optical stability of the $\text{Cs}_2\text{Na}_{0.8}\text{Bi}_{0.8}\text{Mn}_{0.4}\text{Cl}_6$ MCs under high humidity environment will be more beneficial for its future commercial development. Here, 1 mL H_2O was injected directly into $\text{Cs}_2\text{Na}_{0.8}\text{Bi}_{0.8}\text{Mn}_{0.4}\text{Cl}_6$ MCs powder to simulate its working environment under high humidity conditions, followed by the structural and optical stability of $\text{Cs}_2\text{Na}_{0.8}\text{Bi}_{0.8}\text{Mn}_{0.4}\text{Cl}_6$ MCs under this environment was evaluated by recording changes in its XRD patterns, absorbance and PL spectra. Unfortunately, after 1 mL H_2O was injected into

$\text{Cs}_2\text{Na}_{0.8}\text{Bi}_{0.8}\text{Mn}_{0.4}\text{Cl}_6$ MCs powder, the sample remained as a white powder, but its orange–red fluorescence emission under UV excitation was completely quenched (Fig. 3a). Correspondingly, the main crystal phase of the sample was transformed after injecting water, with the characteristic diffraction peak of the pristine $\text{Cs}_2\text{Na}_{0.8}\text{Bi}_{0.8}\text{Mn}_{0.4}\text{Cl}_6$ MCs rapidly weakening and being replaced by a strong diffraction peak of BiOCl (Fig. 3b). This can be explained by the fact that Bi^{3+} in $\text{Cs}_2\text{Na}_{0.8}\text{Bi}_{0.8}\text{Mn}_{0.4}\text{Cl}_6$ would react with H_2O molecules to form BiOCl under high humidity environment, thus causing the decomposition of the main crystal phase, which directly triggered the fluorescence quenching. The transformation of the main crystal phase can be described by the following equation,



A similar phenomenon was reported in a previous study on $\text{Cs}_2\text{AgBiBr}_6$ NCs, where Bi^{3+} in $\text{Cs}_2\text{AgBiBr}_6$ reacted with H_2O molecules to produce BiOBr [28]. Moreover, the optical properties of the $\text{Cs}_2\text{Na}_{0.8}\text{Bi}_{0.8}\text{Mn}_{0.4}\text{Cl}_6$ MCs suffered severe damage. The results revealed that the three distinct absorption peaks of $\text{Cs}_2\text{Na}_{0.8}\text{Bi}_{0.8}\text{Mn}_{0.4}\text{Cl}_6$ MCs disappeared completely with injecting H_2O and were replaced by the absorbance spectrum of the pure phase BiOCl (Fig. 3c). The elimination of the characteristic absorption peak can

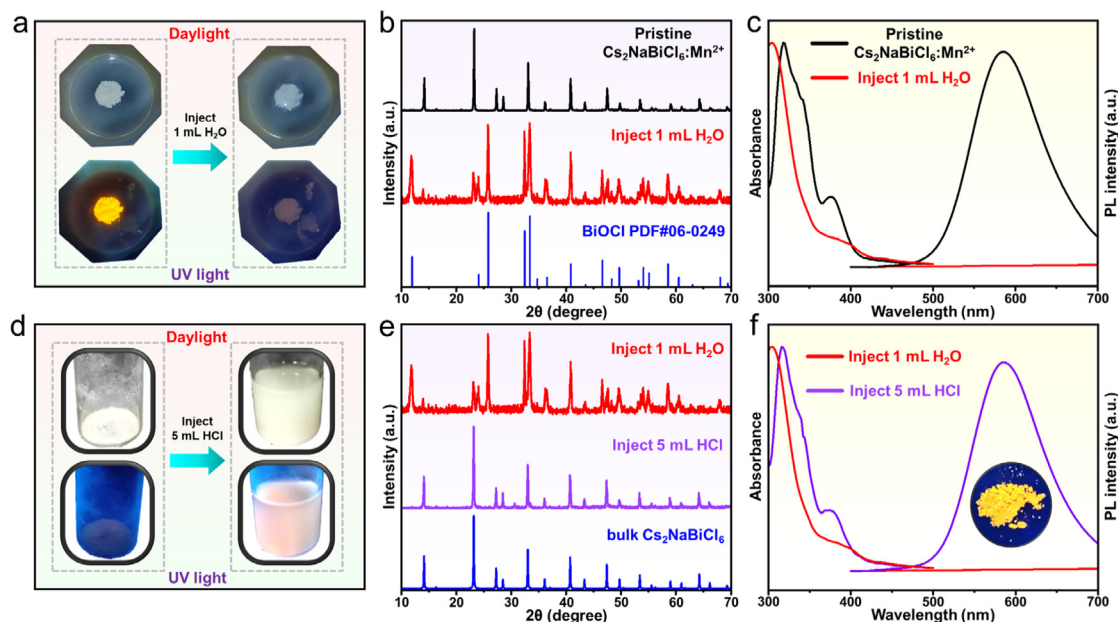
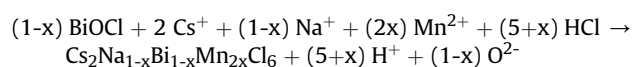


Fig. 3. (a) Photographs of $\text{Cs}_2\text{Na}_{0.8}\text{Bi}_{0.8}\text{Mn}_{0.4}\text{Cl}_6$ MCs under daylight and UV light after injecting 1 mL H_2O . The changes in (b) XRD patterns, (c) absorbance and PL spectra of the samples before and after H_2O injection. Subsequently, (d) photographs of the samples under daylight and UV light after injecting 5 mL HCl again. The changes in (e) XRD patterns, (f) absorbance and PL spectra of the samples before and after HCl injection. The inset in (f) shows a photograph of the final collected powder under UV light. MC, microcrystal; PL, photoluminescence; UV, ultraviolet; XRD, X-ray diffraction.

be attributed to a change in the main crystal phase of sample ($\text{Cs}_2\text{Na}_{0.8}\text{Bi}_{0.8}\text{Mn}_{0.4}\text{Cl}_6 \rightarrow \text{BiOCl}$) (Fig. 3b), where the $[\text{BiCl}_6]^{3-}$ octahedral structure of the pristine $\text{Cs}_2\text{Na}_{0.8}\text{Bi}_{0.8}\text{Mn}_{0.4}\text{Cl}_6$ MCs was destroyed, and the corresponding $6s^2 \rightarrow 6s^1p^1$ transitions would no longer exist. At the same time, the PL property of $\text{Cs}_2\text{Na}_{0.8}\text{Bi}_{0.8}\text{Mn}_{0.4}\text{Cl}_6$ MCs was also totally lost, which was closely linked to the transformation in the crystal phase of the sample. Subsequently, SEM image of the sample after injecting H_2O showed that the octahedral particles of $\text{Cs}_2\text{Na}_{0.8}\text{Bi}_{0.8}\text{Mn}_{0.4}\text{Cl}_6$ MCs were already unobservable (Fig. S5a), and the sample had been transformed into irregular lamellar particles at this time, which again indicated the rapid decomposition of $\text{Cs}_2\text{Na}_{0.8}\text{Bi}_{0.8}\text{Mn}_{0.4}\text{Cl}_6$ MCs after contact with H_2O molecules, directly inhibiting its optical stability under high humidity environments.

Interestingly, the sample after injecting H_2O was dried and re-collected, and it still exhibited no fluorescence properties (Fig. 3d), indicating that the reaction of $\text{Cs}_2\text{Na}_{0.8}\text{Bi}_{0.8}\text{Mn}_{0.4}\text{Cl}_6$ MCs with H_2O molecules was irreversible. Excitingly, the fluorescence properties of the sample were restored by re-injecting 5 mL HCl into the dried sample (Fig. 3d). The XRD pattern of the sample was further monitored and the results showed that the diffraction peak of BiOCl was suppressed, while the characteristic diffraction peak of $\text{Cs}_2\text{Na}_{0.8}\text{Bi}_{0.8}\text{Mn}_{0.4}\text{Cl}_6$ MCs reoccupied the location of the main crystal phase (Fig. 3e). This phenomenon suggested that the sample had again undergone a crystal phase transformation and that BiOCl can be utilized as a reactant for the synthesis of $\text{Cs}_2\text{Na}_{0.8}\text{Bi}_{0.8}\text{Mn}_{0.4}\text{Cl}_6$, which reacted again with Cs^+ , Na^+ , and Mn^{2+} in HCl solvent to obtain $\text{Cs}_2\text{Na}_{0.8}\text{Bi}_{0.8}\text{Mn}_{0.4}\text{Cl}_6$ MCs with fluorescent properties. The transformation again of the main crystal phase can be described by the following equation,



In previous reports, BiOCl had also been utilized by researchers to synthesize $\text{Cs}_2\text{AgBiCl}_6$ MCs [38]. At the same time,

the optical properties of the sample were recovered (Fig. 3f), and the three characteristic absorption peaks of $\text{Cs}_2\text{Na}_{0.8}\text{Bi}_{0.8}\text{Mn}_{0.4}\text{Cl}_6$ MCs were clearly observed in its corresponding absorbance spectrum, and the corresponding PL spectrum also exhibited a noticeable fluorescence emission peak at 585 nm, which was attributed to the re-reaction of the sample to acquire $\text{Cs}_2\text{Na}_{0.8}\text{Bi}_{0.8}\text{Mn}_{0.4}\text{Cl}_6$ MCs after the HCl injection. Additionally, it can be seen that the dried sample also displayed orange–red emission under UV irradiation (inset of Fig. 3f), but its PLQY was only 16.1% and could not be restored to 22.3% of the pristine $\text{Cs}_2\text{Na}_{0.8}\text{Bi}_{0.8}\text{Mn}_{0.4}\text{Cl}_6$ MCs. Finally, SEM image of the sample after injecting HCl indicated that the sample collected was irregularly blocky (Fig. S5b), and unable to revert the pristine octahedral particles, implying that the microscopic morphology modification caused by the reaction of $\text{Cs}_2\text{Na}_{0.8}\text{Bi}_{0.8}\text{Mn}_{0.4}\text{Cl}_6$ MCs with H_2O molecules was permanent. The above test results revealed that $\text{Cs}_2\text{Na}_{0.8}\text{Bi}_{0.8}\text{Mn}_{0.4}\text{Cl}_6$ MCs would rapidly transform into BiOCl after contact with water molecules, accompanied by a quenching of its optical properties, which suggested that $\text{Cs}_2\text{Na}_{0.8}\text{Bi}_{0.8}\text{Mn}_{0.4}\text{Cl}_6$ MCs was not suitable for operation under high humidity environment, severely limiting its development in the field of optoelectronic devices. Therefore, solving the optical instability of $\text{Cs}_2\text{Na}_{0.8}\text{Bi}_{0.8}\text{Mn}_{0.4}\text{Cl}_6$ MCs under high humidity condition will become an integral step for its subsequent commercial development.

Targeting to solve the structural and optical instability of $\text{Cs}_2\text{Na}_{0.8}\text{Bi}_{0.8}\text{Mn}_{0.4}\text{Cl}_6$ MCs under high humidity environment, referring to the previous methods of improving the water stability of lead halide perovskite [39–41], a strategy of surface encapsulation of $\text{Cs}_2\text{Na}_{0.8}\text{Bi}_{0.8}\text{Mn}_{0.4}\text{Cl}_6$ MCs by water stable and highly transparent SiO_2 layer was proposed, which was simple and low-cost. As shown in Fig. 4a, the before prepared $\text{Cs}_2\text{Na}_{0.8}\text{Bi}_{0.8}\text{Mn}_{0.4}\text{Cl}_6$ MCs were dispersed in ethanol absolute, followed by $\text{Si}(\text{OC}_2\text{H}_5)_4$ being injected into the solution by the sol-gel method, which was hydrolyzed in air at room temperature, thereby formed stable $\text{Cs}_2\text{Na}_{0.8}\text{Bi}_{0.8}\text{Mn}_{0.4}\text{Cl}_6@ \text{SiO}_2$ core-shell MCs. Here, the

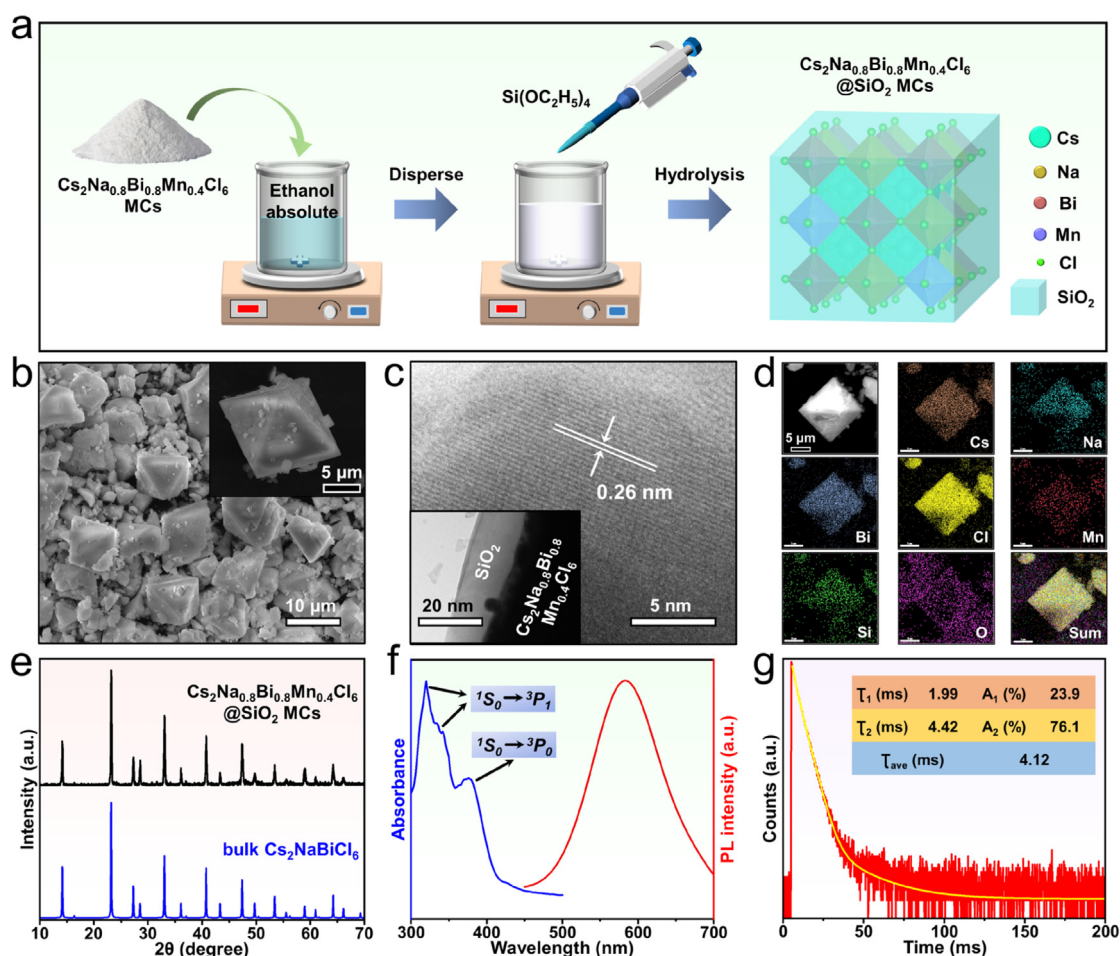


Fig. 4. (a) A schematic diagram for the preparation process of $\text{Cs}_2\text{Na}_{0.8}\text{Bi}_{0.8}\text{Mn}_{0.4}\text{Cl}_6@SiO_2$ MCs. SEM (b) and HRTEM (c) images of $\text{Cs}_2\text{Na}_{0.8}\text{Bi}_{0.8}\text{Mn}_{0.4}\text{Cl}_6@SiO_2$ MCs. (d) Elemental mapping of $\text{Cs}_2\text{Na}_{0.8}\text{Bi}_{0.8}\text{Mn}_{0.4}\text{Cl}_6@SiO_2$ MCs. (e) XRD pattern of $\text{Cs}_2\text{Na}_{0.8}\text{Bi}_{0.8}\text{Mn}_{0.4}\text{Cl}_6@SiO_2$ MCs. (f) Absorbance, PL, and (g) time-resolved PL spectra of $\text{Cs}_2\text{Na}_{0.8}\text{Bi}_{0.8}\text{Mn}_{0.4}\text{Cl}_6@SiO_2$ MCs. The inset in (b) shows the corresponding single MC. The inset in (c) shows the corresponding TEM image. HRTEM, high-resolution transmission electron microscope; MC, microcrystal; PL, photoluminescence; SEM, scanning electron microscope; TEM, transmission electron microscope; XRD, X-ray diffraction.

hydrolysis process of precursor $\text{Si}(\text{OC}_2\text{H}_5)_4$ with water molecules in air can be described as follows [42].



As can be seen from the SEM image, the encapsulation process of SiO_2 did not cause any significant damage to the structure of $\text{Cs}_2\text{Na}_{0.8}\text{Bi}_{0.8}\text{Mn}_{0.4}\text{Cl}_6$ MCs, and the morphology of the sample remained as octahedral particles with an average size of about 10 μm (Fig. 4b). At the same time, the surface of $\text{Cs}_2\text{Na}_{0.8}\text{Bi}_{0.8}\text{Mn}_{0.4}\text{Cl}_6@SiO_2$ MC was no longer smooth, which can be attributed to the encapsulation of the SiO_2 layer on its surface (inset of Fig. 4b). The corresponding TEM image can also clearly observe the existence of a SiO_2 shell on the surface of $\text{Cs}_2\text{Na}_{0.8}\text{Bi}_{0.8}\text{Mn}_{0.4}\text{Cl}_6$ MC (inset of Fig. 4c), with the internal $\text{Cs}_2\text{Na}_{0.8}\text{Bi}_{0.8}\text{Mn}_{0.4}\text{Cl}_6$ MC still exhibiting high crystallinity and a lattice spacing of 0.26 nm (Fig. 4c). Additionally, there were extra Si and O elements being detected in the energy-dispersive spectroscopy spectrum of $\text{Cs}_2\text{Na}_{0.8}\text{Bi}_{0.8}\text{Mn}_{0.4}\text{Cl}_6@SiO_2$ MCs (Fig. S6), and the elemental mapping images also reflected their uniform distribution on the surface of $\text{Cs}_2\text{Na}_{0.8}\text{Bi}_{0.8}\text{Mn}_{0.4}\text{Cl}_6$ (Fig. 4d), which again confirmed that

$\text{Cs}_2\text{Na}_{0.8}\text{Bi}_{0.8}\text{Mn}_{0.4}\text{Cl}_6$ MCs had been completely encapsulated by SiO_2 to obtain stable $\text{Cs}_2\text{Na}_{0.8}\text{Bi}_{0.8}\text{Mn}_{0.4}\text{Cl}_6@SiO_2$ MCs. Subsequently, the XRD pattern indicated that $\text{Cs}_2\text{Na}_{0.8}\text{Bi}_{0.8}\text{Mn}_{0.4}\text{Cl}_6@SiO_2$ MCs after SiO_2 encapsulation maintained the DP structure of bulk $\text{Cs}_2\text{NaBiCl}_6$ (Fig. 4e), which stemmed from the fact that the higher crystallinity of $\text{Cs}_2\text{Na}_{0.8}\text{Bi}_{0.8}\text{Mn}_{0.4}\text{Cl}_6$ MCs completely masked the diffraction peaks of amorphous SiO_2 , implying that its own optical properties were preserved. The absorbance spectrum of $\text{Cs}_2\text{Na}_{0.8}\text{Bi}_{0.8}\text{Mn}_{0.4}\text{Cl}_6@SiO_2$ MCs was basically consistent with $\text{Cs}_2\text{Na}_{0.8}\text{Bi}_{0.8}\text{Mn}_{0.4}\text{Cl}_6$ MCs, the three characteristic absorption peaks were observed (Fig. 4f, blue line), and the PL spectrum also showed a broad PL peak at 585 nm (Fig. 4f, red line), with the corresponding PLQY remaining at 23.5%, these benefited from the high transparent of the surface SiO_2 layer, which allowed the optical properties of $\text{Cs}_2\text{Na}_{0.8}\text{Bi}_{0.8}\text{Mn}_{0.4}\text{Cl}_6$ MCs to be maximally retained. The time-resolved PL spectrum of $\text{Cs}_2\text{Na}_{0.8}\text{Bi}_{0.8}\text{Mn}_{0.4}\text{Cl}_6@SiO_2$ MCs revealed that its PL decay curve was also fitted by a bi-exponential decay function (Fig. 4g), and the results suggested that its average decay lifetime (4.12 ms) was almost identical to the unencapsulated $\text{Cs}_2\text{Na}_{0.8}\text{Bi}_{0.8}\text{Mn}_{0.4}\text{Cl}_6$ MCs (4.08 ms), indicating that the high transmittance SiO_2 was not shielding the light absorption and emission of $\text{Cs}_2\text{Na}_{0.8}\text{Bi}_{0.8}\text{Mn}_{0.4}\text{Cl}_6$, which again supported that encapsulation of SiO_2 did not interfere with the optical properties of $\text{Cs}_2\text{Na}_{0.8}\text{Bi}_{0.8}\text{Mn}_{0.4}\text{Cl}_6$ MCs. From the analysis of these characterization results, it can be concluded that the optical properties of

$\text{Cs}_2\text{Na}_{0.8}\text{Bi}_{0.8}\text{Mn}_{0.4}\text{Cl}_6@/\text{SiO}_2$ MCs after SiO_2 encapsulation were not weakened, it was equally suitable for the exploitation of lead-free DP optoelectronic devices.

Further investigation was carried on the stability of $\text{Cs}_2\text{Na}_{0.8}\text{Bi}_{0.8}\text{Mn}_{0.4}\text{Cl}_6@/\text{SiO}_2$ MCs after encapsulation by SiO_2 under high humidity environment. Similarly, 1 mL H_2O was injected into the $\text{Cs}_2\text{Na}_{0.8}\text{Bi}_{0.8}\text{Mn}_{0.4}\text{Cl}_6@/\text{SiO}_2$ MCs powder to simulate it being exposed to high humidity environment. Surprisingly, the $\text{Cs}_2\text{Na}_{0.8}\text{Bi}_{0.8}\text{Mn}_{0.4}\text{Cl}_6@/\text{SiO}_2$ MCs powder was still able to exhibit strong orange–red light emission under UV light after 1 mL H_2O was injected (Fig. 5a), which stemmed from the SiO_2 encapsulation layer on the surface provided a protective effect for the internal $\text{Cs}_2\text{Na}_{0.8}\text{Bi}_{0.8}\text{Mn}_{0.4}\text{Cl}_6$. A similar phenomenon has been reported in lead halide perovskite, where $\text{CsPbX}_3@/\text{SiO}_2$ encapsulated by SiO_2 showed long-term stability in aqueous solution [43]. No significant secondary phase was detected in the corresponding XRD pattern (Fig. 5b), which reflected the comprehensive encapsulation of $\text{Cs}_2\text{Na}_{0.8}\text{Bi}_{0.8}\text{Mn}_{0.4}\text{Cl}_6$ by SiO_2 so that the crystal phase transformation was not triggered upon contact with H_2O molecules. There is no doubt that the optical properties of $\text{Cs}_2\text{Na}_{0.8}\text{Bi}_{0.8}\text{Mn}_{0.4}\text{Cl}_6@/\text{SiO}_2$ MCs were also not noticeably altered after being injected with H_2O (Fig. 5c). Of these, all the characteristic absorption peaks of $\text{Cs}_2\text{Na}_{0.8}\text{Bi}_{0.8}\text{Mn}_{0.4}\text{Cl}_6@/\text{SiO}_2$ MCs can be monitored in its absorbance spectrum, which benefited from the fact that the $[\text{BiCl}_6]^{3-}$ octahedral structure was preserved, the corresponding PL emission intensity has not been decayed. Meanwhile, the morphology of $\text{Cs}_2\text{Na}_{0.8}\text{Bi}_{0.8}\text{Mn}_{0.4}\text{Cl}_6@/\text{SiO}_2$ MCs was also

maintained as a primitive octahedral particle (Fig. 5d), confirming again that the encapsulation of SiO_2 was very effective, which completely isolated $\text{Cs}_2\text{Na}_{0.8}\text{Bi}_{0.8}\text{Mn}_{0.4}\text{Cl}_6$ from contact with H_2O molecules. In addition, long-term water stability was also an important indicator for optoelectronic materials, so ultra-long-term water stability test was carried to $\text{Cs}_2\text{Na}_{0.8}\text{Bi}_{0.8}\text{Mn}_{0.4}\text{Cl}_6@/\text{SiO}_2$ MCs. The results demonstrated that the optical properties and crystal structure of $\text{Cs}_2\text{Na}_{0.8}\text{Bi}_{0.8}\text{Mn}_{0.4}\text{Cl}_6@/\text{SiO}_2$ MCs did not deteriorate after being stored in aqueous solution for 10 days (Fig. S7a–d), which again reflected that the surface SiO_2 encapsulation layer was very stable, greatly enhancing the competitiveness of $\text{Cs}_2\text{Na}_{0.8}\text{Bi}_{0.8}\text{Mn}_{0.4}\text{Cl}_6@/\text{SiO}_2$ MCs in the future optoelectronic material field. From the above test analysis, it can be concluded that the encapsulation of $\text{Cs}_2\text{Na}_{0.8}\text{Bi}_{0.8}\text{Mn}_{0.4}\text{Cl}_6$ with SiO_2 does effectively improve its stability in aqueous solutions, further supporting that $\text{Cs}_2\text{Na}_{0.8}\text{Bi}_{0.8}\text{Mn}_{0.4}\text{Cl}_6@/\text{SiO}_2$ MCs can be widely applied in various lighting systems with high humidity environments, which will provide a new option for the subsequent development of highly stable lead-free DP optoelectronic devices.

In order to evaluate the stability enhancement effect of the $\text{Cs}_2\text{Na}_{0.8}\text{Bi}_{0.8}\text{Mn}_{0.4}\text{Cl}_6@/\text{SiO}_2$ MCs encapsulated by SiO_2 in practical optoelectronic applications, $\text{Cs}_2\text{Na}_{0.8}\text{Bi}_{0.8}\text{Mn}_{0.4}\text{Cl}_6$ MCs and $\text{Cs}_2\text{Na}_{0.8}\text{Bi}_{0.8}\text{Mn}_{0.4}\text{Cl}_6@/\text{SiO}_2$ MCs were separately coated on the UV chip surface and assembled into high performance orange–red LED devices (Fig. 6a). The LED devices assembled from these two materials both exhibited bright orange–red emission, and the corresponding international commission on illumination diagrams

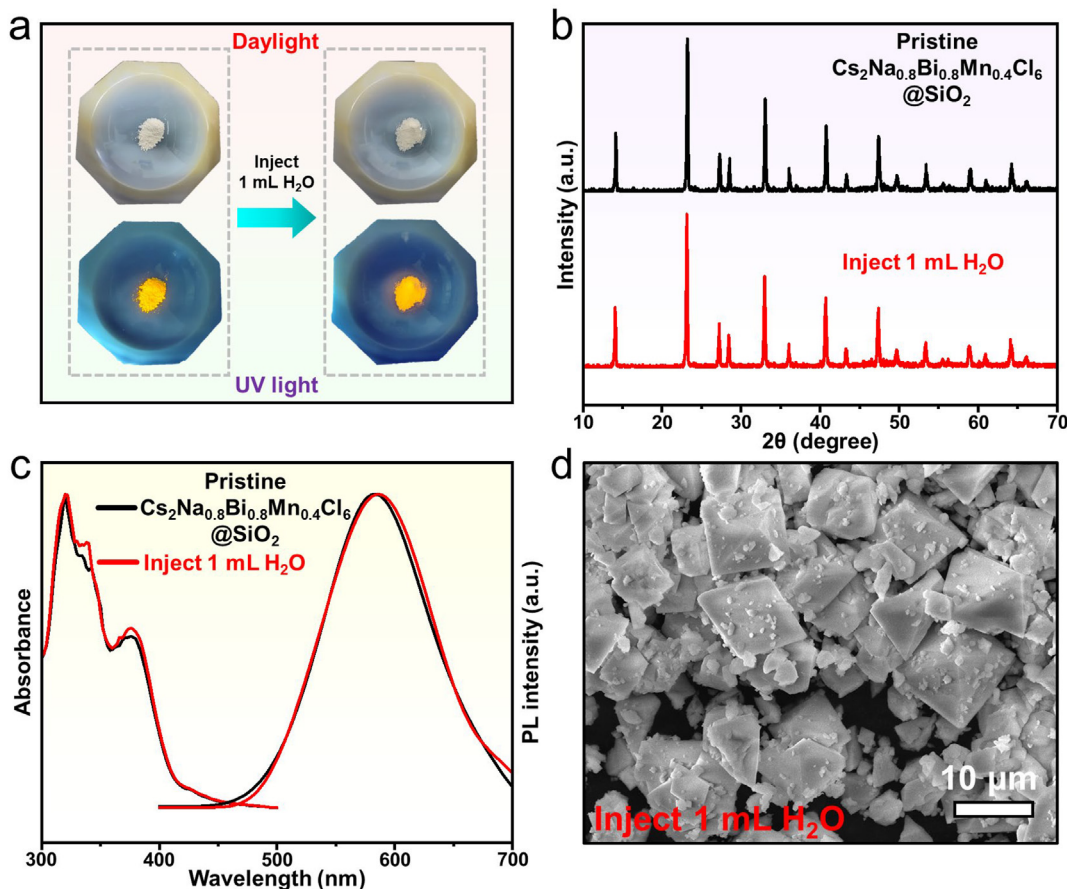


Fig. 5. (a) Photographs of $\text{Cs}_2\text{Na}_{0.8}\text{Bi}_{0.8}\text{Mn}_{0.4}\text{Cl}_6@/\text{SiO}_2$ MCs under daylight and UV light after injecting 1 mL H_2O . The changes in (b) XRD patterns, (c) absorbance and PL spectra of the samples before and after H_2O injection. (d) SEM image of the sample after injecting H_2O . MC, microcrystal; PL, photoluminescence; SEM, scanning electron microscope; UV, ultraviolet; XRD, X-ray diffraction.

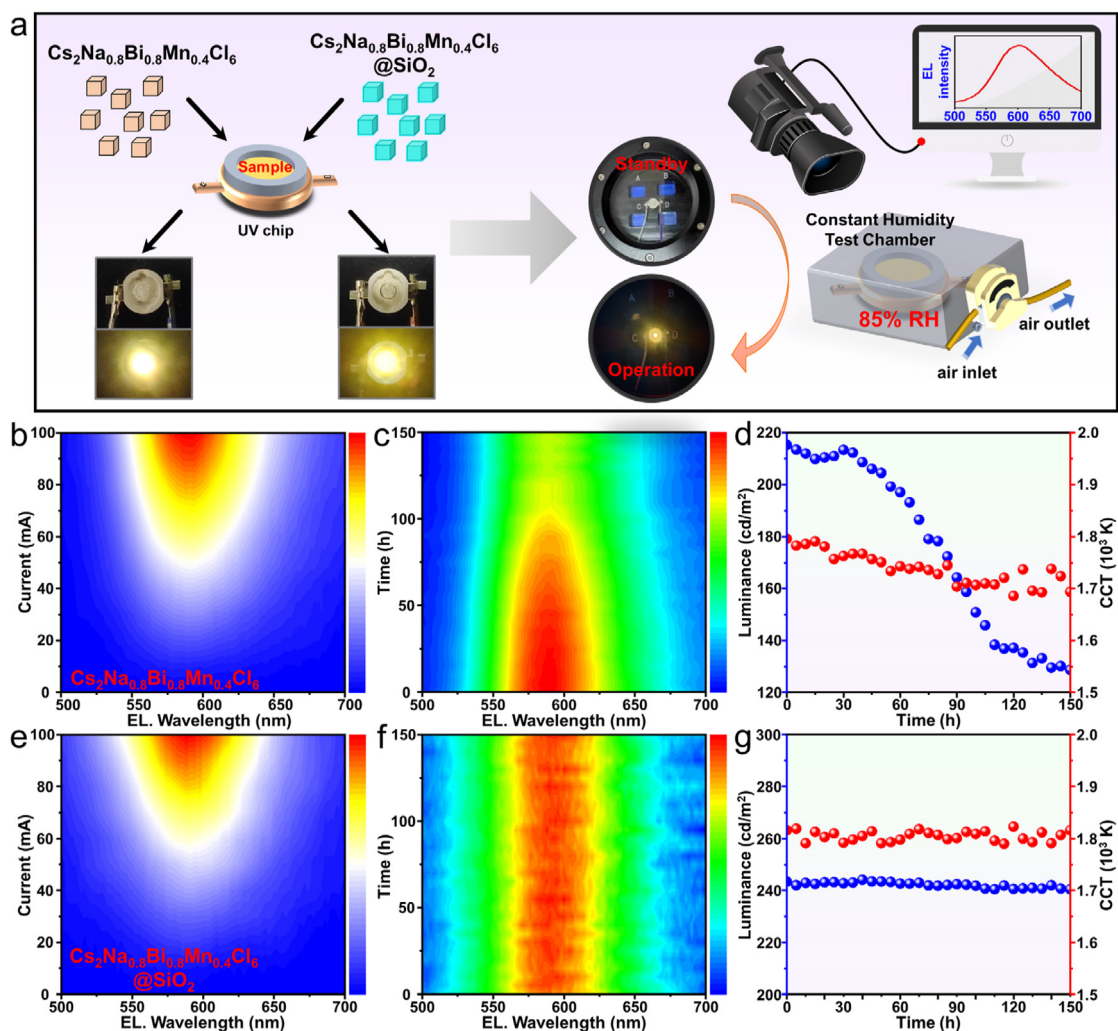


Fig. 6. (a) Schematic diagram of the LED devices assembled with $\text{Cs}_2\text{Na}_{0.8}\text{Bi}_{0.8}\text{Mn}_{0.4}\text{Cl}_6$ MCs and $\text{Cs}_2\text{Na}_{0.8}\text{Bi}_{0.8}\text{Mn}_{0.4}\text{Cl}_6 @ \text{SiO}_2$ MCs respectively, and the operational stability test of LEDs under high humidity (85% RH) conditions. (b), (e) EL spectra of LED devices at different drive currents. Changes in the (c), (f) EL spectra, (d), (g) luminance (blue dot) and CCT (red dot) of the LEDs at different storage times under high humidity environments. (For interpretation of the references to color in this figure legend, the reader is referred to the Web version of this article). CCT, correlated color temperature; EL, electroluminescence; MC, microcrystal; LED, light emitting diode; RH, relative humidity.

revealed their color coordinates located at (0.52, 0.47) and (0.50, 0.48), respectively, both being classified in the orange–red region (Fig. S8a–b), suggesting that the encapsulation of SiO_2 does not cause significant fluctuation in LED light emission. When the drive current was increased from 5 mA to 100 mA, there was no apparent saturation of the emission intensity observed in the electroluminescence (EL) spectra for both LED devices (Fig. 6b, e), and the corresponding device luminance also improved with increased current (Fig. S9a–b, blue dot), indicating that the $\text{Cs}_2\text{Na}_{0.8}\text{Bi}_{0.8}\text{Mn}_{0.4}\text{Cl}_6$ MCs and $\text{Cs}_2\text{Na}_{0.8}\text{Bi}_{0.8}\text{Mn}_{0.4}\text{Cl}_6 @ \text{SiO}_2$ MCs separately assembled LEDs would be suitable for high power lighting and display systems. At the same time, the correlated color temperature (CCT) values of both LED devices were maintained at approximately 1800 K, which was attributed to the fact that their light emission both came from $\text{Cs}_2\text{Na}_{0.8}\text{Bi}_{0.8}\text{Mn}_{0.4}\text{Cl}_6$. Moreover, the corresponding CCT values do not vary drastically with increasing drive current, suggesting that the LEDs keep their high light emission purity at different running powers (Fig. S9a–b, red dot). Especially, the enhancement effect on the stability of optoelectronic devices by SiO_2 encapsulation was evaluated by placing the assembled LEDs in a constant humidity test chamber. In order to probe the working state of the device under extreme humidity, the RH in the test

chamber was maintained at 85%, and the EL spectra and related optoelectronic parameters of the LEDs were recorded at different storage times (Fig. 6a). Among them, the EL intensity decay of the LED assembled with $\text{Cs}_2\text{Na}_{0.8}\text{Bi}_{0.8}\text{Mn}_{0.4}\text{Cl}_6$ MCs was the most obviously with the extended storage time (Fig. 6c), which can be attributed to the fact that $\text{Cs}_2\text{Na}_{0.8}\text{Bi}_{0.8}\text{Mn}_{0.4}\text{Cl}_6$ MCs would be reacted with water molecules under high humidity atmosphere, thereby leading to a weakness in the light emission intensity of the device, and greatly detrimental to the long-term service of the optoelectronic device. At the same time, the luminance of the device also changed significantly as the storage time increased (Fig. 6d, blue dot). During the first 30 h, the luminance of the device stayed essentially at 210 cd/m^2 , which benefited from the lower degree that $\text{Cs}_2\text{Na}_{0.8}\text{Bi}_{0.8}\text{Mn}_{0.4}\text{Cl}_6$ MCs was eroded by water molecules not enough for significant effects on light emission. The luminance of the LED also began to decay as the storage time continued to extend, the $\text{Cs}_2\text{Na}_{0.8}\text{Bi}_{0.8}\text{Mn}_{0.4}\text{Cl}_6$ MCs was seriously affected by the erosion of water molecules at this point, and a large amount of BiOCl without optical properties attached to the UV chip surface, hindering the light emission of the device, and the luminance had decayed to 140 cd/m^2 at storage for 105 h. The decaying trend in the luminance of the device became slower as the storage

time was further extended, which can be attributed to the fact that the BiOCl covered on the surface was able to isolate the water molecules, acting as a protection for the $\text{Cs}_2\text{Na}_{0.8}\text{Bi}_{0.8}\text{Mn}_{0.4}\text{Cl}_6$ MCs in the deeper layers. The luminance of LEDs was only 130 cd/m^2 after being stored at 85% RH for 150 h, corresponding the CCT value shifted to 1700 K (Fig. 6d, red dot), which seriously inconsistent with the stability requirements of modern optoelectronic devices, thus $\text{Cs}_2\text{Na}_{0.8}\text{Bi}_{0.8}\text{Mn}_{0.4}\text{Cl}_6$ MCs was unsuitable as a candidate for a new optoelectronic material. In stark contrast, the EL intensity of the LED assembled with $\text{Cs}_2\text{Na}_{0.8}\text{Bi}_{0.8}\text{Mn}_{0.4}\text{Cl}_6@ \text{SiO}_2$ MCs barely changed in 85% RH environment with storage time elevated (Fig. 6f), which was facilitated by the tight encapsulation of SiO_2 , completely inhibiting the erosion of $\text{Cs}_2\text{Na}_{0.8}\text{Bi}_{0.8}\text{Mn}_{0.4}\text{Cl}_6$ by water molecules. Strikingly, the optoelectronic parameters of the device were kept stable during the entire period of storage for 150 h, with the luminance of this LED maintained essentially at a high emission state of 240 cd/m^2 (Fig. 6g, blue dot), and the corresponding CCT value fluctuating in a small range around 1800 K (Fig. 6g, red dot). Based on the above practical work performance of the optoelectronic devices, the LED assembled with $\text{Cs}_2\text{Na}_{0.8}\text{Bi}_{0.8}\text{Mn}_{0.4}\text{Cl}_6@ \text{SiO}_2$ MCs maintained consistently stable optical output under high humidity of 85% RH, indicating that it can be better adapted to lighting and display systems under extreme environments, which provided a new avenue for the subsequent development of efficient and stable lead-free DP devices.

3. Conclusion

In summary, a series of $\text{Cs}_2\text{Na}_{1-x}\text{Bi}_{1-x}\text{Mn}_{2x}\text{Cl}_6$ MCs with different Mn^{2+} content was acquired by a simple solution method at room temperature, and the stability of $\text{Cs}_2\text{Na}_{0.8}\text{Bi}_{0.8}\text{Mn}_{0.4}\text{Cl}_6$ MCs, the most optically prominent performer, was investigated under high humidity environment. Unfortunately, the host structure of $\text{Cs}_2\text{Na}_{0.8}\text{Bi}_{0.8}\text{Mn}_{0.4}\text{Cl}_6$ MCs rapidly transformed to BiOCl in aqueous solution, accompanied by the quenching of its orange-red PL emission, indicating that $\text{Cs}_2\text{Na}_{1-x}\text{Bi}_{1-x}\text{Mn}_{2x}\text{Cl}_6$ MCs was unsuitable for optoelectronic applications under high humidity environment. Interestingly, the fluorescent properties were restored again by adding HCl solution to the destroyed product, but it was not possible to recover the initial intensity, and the main crystal phase was again transformed into $\text{Cs}_2\text{Na}_{0.8}\text{Bi}_{0.8}\text{Mn}_{0.4}\text{Cl}_6$ MCs, indicating that BiOCl can also be used as a reactant for the preparation of $\text{Cs}_2\text{Na}_{1-x}\text{Bi}_{1-x}\text{Mn}_{2x}\text{Cl}_6$ MCs. Based on this, it was proposed that $\text{Cs}_2\text{Na}_{0.8}\text{Bi}_{0.8}\text{Mn}_{0.4}\text{Cl}_6@ \text{SiO}_2$ MCs core-shell MCs were fabricated by surface encapsulation with water stable and highly transparent SiO_2 , and its optical properties were not decayed after being stored in aqueous solution for 10 days, benefiting from the effective isolation of water molecules by the SiO_2 encapsulation layer. At the same time, the LED devices assembled with $\text{Cs}_2\text{Na}_{0.8}\text{Bi}_{0.8}\text{Mn}_{0.4}\text{Cl}_6@ \text{SiO}_2$ MCs were stored for 150 h under high humidity environment (85% RH), its lighting output remained constant. We believe that this strategy of SiO_2 surface encapsulation will significantly improve the stability of lead-free DP materials, paving the way for the development of subsequent optoelectronic devices under extreme environments.

Credit author statement

Jindou Shi: Conceptualization, Investigation, Methodology, Data curation, Formal analysis, Writing original draft. **Minqiang Wang:** Funding acquisition, Project administration, Supervision, Writing-review & editing. **Chen Zhang:** Investigation. **Junnan Wang:** Investigation, Data curation. **Yun Zhou:** Investigation. **Youlong Xu:** Investigation, Data curation. **Nikolai V. Gaponenko:** Conceptualization, Data curation.

Declaration of competing interest

The authors declare that they have no known competing financial interests or personal relationships that could have appeared to influence the work reported in this paper.

Data availability

No data were used for the research described in the article.

Acknowledgments

This work was supported by the National Key R&D Program of China (2022YFE0122500 and 2019YFB1503200), National Natural Science Foundation of China (NSFC, 52161145103 and 61774124), and 111 Program (No. B14040), and Shaanxi Provincial Key Research and Development Program (No. 2021GXLH-Z-084). The authors thank Ms. Dan He at Instrument Analysis Center of Xi'an Jiaotong University for her the help with the time-resolved PL analysis.

Appendix A. Supplementary data

Supplementary data to this article can be found online at <https://doi.org/10.1016/j.mtchem.2023.101480>.

References

- [1] S. Seth, T. Ahmed, A. De, A. Samanta, Tackling the defects, stability, and photoluminescence of CsPbX_3 perovskite nanocrystals, *ACS Energy Lett.* 4 (2019) 1610–1618, <https://doi.org/10.1021/acseenergylett.9b00849>.
- [2] K. Zhang, J. Zhao, Q.S. Hu, S.J. Yang, X.X. Zhu, Y.Q. Zhang, R.Q. Huang, Y.F. Ma, Z.X. Wang, Z.W. Ouyang, J.B. Han, Y.B. Han, J. Tang, W. Tong, L. Zhang, T.Y. Zhai, Room-temperature magnetic field effect on excitonic photoluminescence in perovskite nanocrystals, *Adv. Mater.* 33 (2021), 2008225, <https://doi.org/10.1002/adma.202008225>.
- [3] H. Lee, J.Y. Woo, D.Y. Park, I. Jo, J. Park, Y. Lee, Y. Koo, J. Choi, H. Kim, Y.H. Kim, M.S. Jeong, S. Jeong, K.D. Park, Tip-induced strain engineering of a single metal halide perovskite quantum dot, *ACS Nano* 15 (2021) 9057–9064, <https://doi.org/10.1021/acsnano.1c02182>.
- [4] J.D. Shi, W.Y. Ge, Y. Tian, M.M. Xu, W.X. Gao, Y.T. Wu, Enhanced stability of all-inorganic perovskite light-emitting diodes by a facile liquid annealing strategy, *Small* 17 (2021), 200656, <https://doi.org/10.1002/sml.202006568>.
- [5] S.S. Mali, J.V. Patil, P.S. Shinde, G. de Miguel, C.K. Hong, Fully air-processed dynamic hot-air-assisted $\text{M:CsPbI}_2\text{Br}$ ($\text{M: Eu}^{2+}, \text{In}^{3+}$) for stable inorganic perovskite solar cells, *Matter* 4 (2021), <https://doi.org/10.1016/j.matt.2020.11.008>.
- [6] J.R. Zhang, G. Hodes, Z.W. Jin, S.Z. Liu, All-inorganic CsPbX_3 perovskite solar cells: progress and prospects, *Angew. Chem. Int. Ed.* 58 (2019) 15596–15618, <https://doi.org/10.1002/anie.201901081>.
- [7] M.G. Gong, R. Sakidja, R. Goul, D. Ewing, M. Casper, A. Stramel, A. Elliot, J.Z. Wu, High-performance all-inorganic CsPbCl_3 perovskite nanocrystal photodetectors with superior stability, *ACS Nano* 13 (2019) 1772–1783, <https://doi.org/10.1021/acsnano.8b07850>.
- [8] Y. Liu, J.Y. Cui, K. Du, H. Tian, Z.F. He, Q.H. Zhou, Z.L. Yang, Y.Z. Deng, D. Chen, X.B. Zuo, Y. Ren, L. Wang, H.M. Zhu, B.D. Zhao, D.W. Di, J.P. Wang, R.H. Friend, Y.Z. Jin, Efficient blue light-emitting diodes based on quantum-confined bromide perovskite nanostructures, *Nat. Photon.* 13 (2019) 760, <https://doi.org/10.1038/s41566-019-0505-4>.
- [9] T.H. Han, K.Y. Jang, Y.T. Dong, R.H. Friend, E.H. Sargent, T.W. Lee, A roadmap for the commercialization of perovskite light emitters, *Nat. Rev. Mater.* 7 (2022) 757–777, <https://doi.org/10.1038/s41578-022-00459-4>.
- [10] B. Yang, K.L. Han, Charge-carrier dynamics of lead-free halide perovskite nanocrystals, *Acc. Chem. Res.* 52 (11) (2019) 3188–3198, <https://doi.org/10.1021/acs.accounts.9b00422>.
- [11] J.W. Han, S.H. Hwang, M.J. Seol, S.Y. Kim, Recent patterning methods for halide perovskite nanoparticles, *Adv. Opt. Mater.* 10 (2022), 2200534, <https://doi.org/10.1002/adom.202200534>.
- [12] A. Dutta, M.K. Vyas, K. Bhowmik, J. Ota, S.K. Hait, K. Chandrasekaran, D. Saxena, S.S.V. Ramakumar, Phase sensitivity of all-inorganic lead halide perovskite nanocrystals, *ACS Mater. Lett.* (2022) 2106–2124, <https://doi.org/10.1021/acsmaterialslett.2c00544>.
- [13] C.T. Kang, H.S. Rao, Y.P. Fang, J.J. Zeng, Z.X. Pan, X.H. Zhong, Antioxidative stannous oxalate derived lead-free stable CsSnX_3 ($\text{X}=\text{Cl}, \text{Br}, \text{and I}$) perovskite nanocrystals, *Angew. Chem. Int. Ed.* 60 (2021) 660–665, <https://doi.org/10.1002/anie.202011569>.

- [14] J. Chen, Z.Y. Luo, Y.P. Fu, X.X. Wang, K.J. Czech, S.S. Shen, L.J. Guo, J.C. Wright, A.L. Pan, S. Jin, Tin(IV)-tolerant vapor-phase growth and photophysical properties of aligned cesium tin halide perovskite (CsSnX_3 ; X = Br, I) nanowires, *ACS Energy Lett.* 4 (2019) 1045–1052, <https://doi.org/10.1021/acsenergylett.9b00543>.
- [15] L. Men, B.A. Rosales, N.E. Gentry, S.D. Cady, J. Vela, Lead-free semiconductors: soft chemistry, dimensionality control, and manganese-doping of germanium halide perovskites, *Chemnanomat* 5 (2019) 334–339, <https://doi.org/10.1002/cnma.201800497>.
- [16] W.H. Ning, F. Gao, Structural and functional diversity in lead-free halide perovskite materials, *Adv. Mater.* 31 (22) (2019), 1900326, <https://doi.org/10.1002/adma.201900326>.
- [17] F. Igbari, Z.K. Wang, L.S. Liao, Progress of lead-free halide double perovskites, *Adv. Energy Mater.* 9 (12) (2019), 1803150, <https://doi.org/10.1002/aenm.201803150>.
- [18] Z.W. Xiao, Z.N. Song, Y.F. Yan, From lead halide perovskites to lead-free metal halide perovskites and perovskite derivatives, *Adv. Mater.* 31 (2019), 1803792, <https://doi.org/10.1002/adma.201803792>.
- [19] Y. Liu, A. Nag, L. Manna, Z.G. Xia, Lead-free double perovskite $\text{Cs}_2\text{AgInCl}_6$, *Angew. Chem. Int. Ed.* 60 (2021) 11592–11603, <https://doi.org/10.1002/anie.202011833>.
- [20] L. Zhou, Y.F. Xu, B.X. Chen, D.B. Kuang, C.Y. Su, Synthesis and photocatalytic application of stable lead-free $\text{Cs}_2\text{AgBiBr}_6$ perovskite nanocrystals, *Small* 14 (2018), 1703762, <https://doi.org/10.1002/sml.201703762>.
- [21] K.N. Nandha, A. Nag, Synthesis and luminescence of Mn-doped $\text{Cs}_2\text{AgInCl}_6$ double perovskites, *Chem. Commun.* 54 (41) (2018) 5205–5208, <https://doi.org/10.1039/c8cc01982g>.
- [22] D.X. Zhu, J. Zito, V. Pinchetti, Z.Y. Dang, A. Olivati, L. Pasquale, A.W. Tang, M.L. Zaffalon, F. Meinardi, I. Infante, L. De Trizio, L. Manna, S. Brovelli, Compositional tuning of carrier dynamics in $\text{Cs}_2\text{Na}_{1-x}\text{Ag}_x\text{BiCl}_6$ double-perovskite nanocrystals, *ACS Energy Lett.* 5 (2020) 1840–1847, <https://doi.org/10.1021/acsenergylett.0c00914>.
- [23] J.D. Majher, M.B. Gray, T.A. Strom, P.M. Woodward, $\text{Cs}_2\text{NaBiCl}_6:\text{Mn}^{2+}$ – a new orange-red halide double perovskite phosphor, *Chem. Mater.* 31 (2019) 1738–1744, <https://doi.org/10.1021/acs.chemmater.8b05280>.
- [24] M.M. Yao, L. Wang, J.S. Yao, K.H. Wang, C. Chen, B.S. Zhu, J.N. Yang, J.J. Wang, W.P. Xu, Q. Zhang, H.B. Yao, Improving lead-free double perovskite $\text{Cs}_2\text{NaBiCl}_6$ nanocrystal optical properties via ion doping, *Adv. Opt. Mater.* 8 (2020), 1901919, <https://doi.org/10.1002/adom.201901919>.
- [25] M. Jeevaraj, S. Sudhakar, P. Devendran, N. Nallamuthu, N.D. Jayaram, M.K. Kumar, Structural, optical and charge density investigations on lead free Mn^{2+} doped $\text{Cs}_2\text{NaBiCl}_6$ double perovskite microcrystals, *Mater. Today Commun.* 33 (2022), 104715, <https://doi.org/10.1016/j.mtcomm.2022.104715>.
- [26] M. Wang, H.X. Sun, F.R. Cao, W. Tian, L. Li, Moisture-triggered self-healing flexible perovskite photodetectors with excellent mechanical stability, *Adv. Mater.* 33 (2021), 2100625, <https://doi.org/10.1002/adma.202100625>.
- [27] Y.C. Zhang, Y.S. Zhao, D. Wu, J.L. Xue, Y. Qiu, M. Liao, Q.B. Pei, M.S. Goorsky, X.M. He, Homogeneous freestanding luminescent perovskite organogel with superior water stability, *Adv. Mater.* 31 (2019), 1902928, <https://doi.org/10.1002/adma.201902928>.
- [28] Q.Q. Fan, S.Y. Wei, J.Z. Ma, W.B. Zhang, L. Wen, Water-driven boost in the visible light photocatalytic performance of $\text{Cs}_2\text{AgBiBr}_6$ double perovskite nanocrystals, *J. Mater. Chem.* 10 (2022) 14923–14932, <https://doi.org/10.1039/d2ta03217a>.
- [29] S.Q. Fang, T.C. Lang, T. Han, M.S. Cai, S.X. Cao, L.L. Peng, B.T. Liu, Y. Zhong, A.N. Yakovlev, V.I. Korepanov, A novel efficient single-phase dual-emission phosphor with high resemblance to the photosynthetic spectrum of chlorophyll A and B, *J. Mater. Chem. C* 8 (2020) 6245–6253, <https://doi.org/10.1039/d0tc00811g>.
- [30] S. Fang, T. Wang, S. He, T. Lang, T. Han, M. Cai, B. Liu, L. Peng, S. Cao, V.I. Korepanov, A.N. Yakovlev, Evolution of a snowflake-like Mn^{2+} doped $\text{Cs}_2\text{NaBiCl}_6$ nanosheet phosphor driven by cation exchange, *SSRN Electron. J.* (2021) 1–32, <https://doi.org/10.2139/ssrn.3967541>.
- [31] J.T. Jiang, G.M. Niu, L.Z. Sui, X.W. Wang, Y.T. Zhang, C. Li, G.R. Wu, K.J. Yuan, X.M. Yang, Transformation between the dark and bright self-trapped excitons in lead-free double-perovskite $\text{Cs}_2\text{NaBiCl}_6$ under pressure, *J. Phys. Chem. Lett.* 12 (2021) 7285–7292, <https://doi.org/10.1021/acs.jpcl.1c02072>.
- [32] S. Wang, J. Qi, S.V. Kershaw, A.L. Rogach, Co-doping of cerium and bismuth into lead-free double perovskite $\text{Cs}_2\text{AgInCl}_6$ nanocrystals results in improved photoluminescence efficiency, *ACS Nanosci. Au* 2 (2021) 93–101, <https://doi.org/10.1021/acsnanosci.1c00028>.
- [33] N. Chen, T. Cai, W.H. Li, K. Hills-Kimball, H.J. Yang, M.D. Que, Y. Nagaoka, Z.Y. Liu, D. Yang, A.G. Dong, C.Y. Xu, R. Zia, O. Chen, Yb- and Mn-doped lead-free double perovskite $\text{Cs}_2\text{AgBiX}_6$ (X = Cl⁻, Br⁻) nanocrystals, *ACS Appl. Mater. Int.* 11 (2019) 16855–16863, <https://doi.org/10.1021/acsaami.9b02367>.
- [34] H. Arfin, A.S. Kshirsagar, J. Kaur, B. Mondal, Z.G. Xia, S. Chakraborty, A. Nag, ns(2) electron (Bi^{3+} and Sb^{3+}) doping in lead-free metal halide perovskite derivatives, *Chem. Mater.* 32 (2020) 10255–10267, <https://doi.org/10.1021/acs.chemmater.0c03394>.
- [35] S. Saikia, A. Joshi, H. Arfin, S. Badola, S. Saha, A. Nag, Sb^{3+} - Er^{3+} -codoped $\text{Cs}_2\text{NaInCl}_6$ for emitting blue and short-wave infrared radiation, *Angew. Chem. Int. Ed.* 61 (2022), e202201628, <https://doi.org/10.1002/anie.202201628>.
- [36] L.M. Chen, W.Y. Yang, H. Fu, W.N. Liu, G. Shao, B. Tang, J.J. Zheng, Mn^{2+} -doped $\text{Cs}_2\text{NaInCl}_6$ double perovskites and their photoluminescence properties, *J. Mater. Sci.* 56 (2021) 8048–8059, <https://doi.org/10.1007/s10853-021-05822-4>.
- [37] R.S. Zeng, L.L. Zhang, Y. Xue, B. Ke, Z. Zhao, D. Huang, Q.L. Wei, W.C. Zhou, B.S. Zou, Highly efficient blue emission from self-trapped excitons in stable Sb^{3+} -doped $\text{Cs}_2\text{NaInCl}_6$ double perovskites, *J. Phys. Chem. Lett.* 11 (6) (2020) 2053–2061, <https://doi.org/10.1021/acs.jpcl.0c00330>.
- [38] S. Ghosh, G.K. Nim, P. Bansal, P. Kar, Investigating the property of water driven lead-free stable inorganic halide double perovskites, *J. Colloid Interf. Sci.* 582 (2021) 1223–1230, <https://doi.org/10.1016/j.jcis.2020.08.114>.
- [39] J.D. Shi, M.Q. Wang, H. Wang, C. Zhang, Y.Q. Ji, J.N. Wang, Y. Zhou, A.S. Bhatti, Preparation of ultra-stable and environmentally friendly $\text{CsPbBr}_3/\text{ZrO}_2/\text{PS}$ composite films for white light-emitting diodes, *Nanoscale* 14 (2022) 16548–16559, <https://doi.org/10.1039/d2nr04255j>.
- [40] Y.Q. Ji, M.Q. Wang, Z. Yang, H. Wang, M.A. Padiyar, J.D. Shi, H.W. Qu, A.S. Bhatti, In situ synthesis of ultra stable TiO_2 coating Rb^{+} -doped red emitting CsPbBr_3 perovskite quantum dots, *J. Phys. Chem. C* 126 (2022) 1542–1551, <https://doi.org/10.1021/acs.jpcc.1c09945>.
- [41] J.D. Shi, W.Y. Ge, W.X. Gao, M.M. Xu, J.F. Zhu, Y.X. Li, Enhanced thermal stability of halide perovskite CsPbX_3 nanocrystals by a facile TPU encapsulation, *Adv. Opt. Mater.* 8 (2020), 1901516, <https://doi.org/10.1002/adom.201901516>.
- [42] W.Z. Lv, L. Li, M.C. Xu, J.X. Hong, X.X. Tang, L.G. Xu, Y.H. Wu, R. Zhu, R.F. Chen, W. Huang, Improving the stability of metal halide perovskite quantum dots by encapsulation, *Adv. Mater.* 31 (2019), 1900682, <https://doi.org/10.1002/adma.201900682>.
- [43] N. Ding, D.L. Zhou, X.K. Sun, W. Xu, H.W. Xu, G.C. Pan, D.Y. Li, S. Zhang, B. Dong, H.W. Song, Highly stable and water-soluble monodisperse $\text{CsPbX}_3/\text{SiO}_2$ nanocomposites for white-LED and cells imaging, *Nanotechnology* 29 (2018), 345703, <https://doi.org/10.1088/1361-6528/Aac84d>.